

Comprehensive scenario for single-crystal growth and doping dependence of resistivity and anisotropic upper critical fields in $(\text{Ba}_{1-x}\text{K}_x)\text{Fe}_2\text{As}_2$ ($0.22 \leq x \leq 1$)

Y. Liu,^{1,*} M. A. Tanatar,^{1,2,†} W. E. Straszheim,^{1,3} B. Jensen,¹ K. W. Dennis,¹ R. W. McCallum,^{1,4} V. G. Kogan,^{1,2} R. Prozorov,^{1,2} and T. A. Lograsso^{1,4}

¹*Division of Materials Sciences and Engineering, Ames Laboratory, Ames, Iowa 50011, USA*

²*Department of Physics and Astronomy, Iowa State University, Ames, Iowa 50011, USA*

³*Materials Analysis and Research Laboratory, Iowa State University, Ames, Iowa 50011, USA*

⁴*Department of Materials Science and Engineering, Iowa State University, Ames, Iowa 50011, USA*

(Received 2 March 2014; revised manuscript received 27 March 2014; published 7 April 2014)

Large high-quality single crystals of hole-doped iron-based superconductor $(\text{Ba}_{1-x}\text{K}_x)\text{Fe}_2\text{As}_2$ were grown over a broad composition range $0.22 \leq x \leq 1$ by inverted temperature gradient method. We found that high soaking temperature, fast cooling rate, and an adjusted temperature window of the growth are necessary to obtain single crystals of heavily K-doped crystals ($0.65 \leq x \leq 0.92$) with narrow compositional distributions as revealed by sharp superconducting transitions in magnetization measurements and close to 100% superconducting volume fraction. The crystals were extensively characterized by x-ray and compositional analysis, revealing monotonic evolution of the c -axis crystal lattice parameter with K substitution. Quantitative measurements of the temperature-dependent in-plane resistivity $\rho(T)$ found doping-independent, constant within error bars, resistivity at room temperature, $\rho(300\text{ K})$, in sharp contrast with the significant doping dependence in electron and isovalent substituted BaFe_2As_2 based compositions. The shape of the temperature-dependent resistivity, $\rho(T)$, shows systematic doping-evolution, being close to T^2 in overdoped and revealing significant contribution of the T -linear component at optimum doping. The slope of the upper critical field, dH_{c2}/dT , scales linearly with T_c for both $H \parallel c$, $H_{c2,c}$, and $H \parallel ab$, $H_{c2,ab}$. The anisotropy of the upper critical field $\gamma \equiv H_{c2,ab}/H_{c2,c}$ determined near zero-field T_c increases from ~ 2 to 4–5 with increasing K doping level from optimal $x \sim 0.4$ to strongly overdoped $x = 1$.

DOI: [10.1103/PhysRevB.89.134504](https://doi.org/10.1103/PhysRevB.89.134504)

PACS number(s): 74.70.Xa, 74.62.Dh, 74.25.Dw

I. INTRODUCTION

Superconductivity in $(\text{Ba}_{1-x}\text{K}_x)\text{Fe}_2\text{As}_2$ (BaK122 in the following) with transition temperature T_c as high as 38 K was found by Rotter *et al.* [1] very soon after discovery of high-temperature superconductivity in $\text{LaFeAs}(\text{O},\text{F})$ by Hosono group [2]. It was found later that superconductivity in BaFe_2As_2 can be also induced by electron doping on partial substitution of Fe atoms with aliovalent Co [3] and Ni [4], by isovalent substitution of Ru atoms at Fe sites [5] and P atoms at As sites [6], or by application of pressure [7].

In both families of compounds, the superconductivity has maximum T_c close to a point where the antiferromagnetic order of the parent compounds BaFe_2As_2 and LaFeAsO , respectively, is suppressed, prompting intense discussion about the relation of superconductivity and magnetism and potentially magnetic mechanism of superconducting pairing [8–12]. A characteristic feature of the scenario, suggested for magnetically mediated superconductivity [13–15], is systematic doping evolution of all electronic properties, in particular, of electrical resistivity. Superconducting T_c has maximum at a point where the line of the second-order magnetic transition goes to $T = 0$ (quantum critical point, QCP). Temperature-dependent resistivity gradually transforms from T^2 expected in Fermi liquid theory of a metal away from QCP to T linear at the QCP. In the transformation range, $\rho(T)$ can be described with a second-order polynomial, with the magnitude

of T -linear term scaling with superconducting T_c [12]. In iron-based superconductors, this scenario works very well in isoelectron doped BaP122 [16–18]. Here maximum T_c is indeed observed at $x = 0.33$, close to doping-tuned magnetic QCP, and signatures of QCP are found in both normal [16–18] and superconducting [19] states, with resistivity at optimal doping being T linear for both in-plane [16] and interplane [20] transport. Deviations from this scenario are not very pronounced in electron-doped BaCo122 . Here, maximum T_c is observed close to a composition where $T_N(x)$ extrapolates to zero, though the actual line shows slope sign change on approaching $T = 0$ and reentrance of the tetragonal phase [21]. The temperature-dependent in-plane resistivity is close to T linear at optimal doping and transforms to T^2 in the overdoped regime, while the interplane resistivity shows limited range of T -linear dependence, terminated at high temperature by a broad crossover [22–25] due to pseudogap. The resistivity anisotropy $\gamma_\rho \equiv \rho_c/\rho_a$ scales with the anisotropy of the upper critical field $\gamma_H \equiv H_{c2,ab}/H_{c2,c}$ [22] with $\gamma_\rho = \gamma_H^2$. The $\gamma_H(x)$ changes steplike between underdoped and overdoped regions of the dome [26,27], due to Fermi surface topology change (Lifshits transition) [28].

Contrary to the cases of isoelectron substitution and electron doping, no systematic studies of the temperature-dependent resistivity and anisotropic properties of hole-doped BaK122 system were reported so far. Studies were performed in the underdoped, $x < 0.4$ [29,30] compositions, for which high-quality single crystals can be grown from FeAs flux [31], or in heavily overdoped range $x > 0.76$ [32], where crystals were prepared from KAs flux [33]. Crystals of BaK122 can be also grown from Sn flux [34], however, their properties are

*yliu@ameslab.gov

†tanatar@ameslab.gov

notably affected by Sn inclusions at sub-percent level and will not be discussed here.

In BaK122, the superconductivity appears on sufficient suppression of antiferromagnetic order, for $x > \approx 0.15$, while magnetism is completely suppressed by $x \approx 0.25$ [35,36], revealing a range of bulk coexistence. The doping edge of magnetism corresponds to $T_c \sim 27$ K [30], notably lower than the highest $T_c \approx 38$ K observed at optimal doping $x \approx 0.4$, away from concentration boundary of magnetism suppression. The $T_c(x)$ dependence for x in the range 0.4 to 0.6 is nearly flat [37]. The superconductivity is observed in the whole substitution range up to $x = 1$ with steady decrease of T_c down to 3.7 K in the end member KFe_2As_2 ($x = 1$).

Broad crossover in the temperature-dependent resistivity is observed in in-plane transport in single crystals of BaK122 at doping close to optimal [38], similar to pure stoichiometric KFe_2As_2 (K122) [39–43]. Explanation of the crossover was suggested as arising from multi-band effects [38], with contribution of two conductivity channels, as found in optical studies [44] with nearly temperature-independent and strongly temperature dependent resistivities, respectively. The maximum in $\rho_a(T)$ of BaK122 was discussed by Gasparov *et al.* [45] as arising from phonon-assisted scattering between two Fermi-surface sheets.

The information about the doping-evolution of the upper critical field in hole-doped BaK122 is scattered. Very high upper critical fields were reported for close to optimally doped compositions [45–47], in addition, these compositions are characterized by rather small critical field anisotropy. In another doping regime, close to $x = 1$, very unusual behavior of the upper critical fields is found. In KFe_2As_2 , the orbital H_{c2} found in $H \parallel c$ configuration, is close to T linear [40]. The slope of the dependence does not depend on T_c suppression with impurities [43]. In configuration with magnetic field parallel to the plane, $H \parallel ab$, the upper critical field is Pauli limited, as suggested both by the difference in the shape of the phase diagram and quite sharp changes at H_{c2} [48]. Heat capacity study in $H \parallel a$ configuration, however, had not found first order transition [49], but rather suggested multiband Fulde-Ferrel-Larkin-Ovchinnikov (FFLO [50,51]) state [52]. In slightly less doped material with $x = 0.93$, ($T_c \sim 8$ K) hysteresis is observed in the field-tuned resistive transition curves in $H \parallel ab$ configuration at temperatures below 1 K, which can be attributed to a first-order superconducting transition due to paramagnetic effect [53]. More systematic studies of the anisotropic H_{c2} in BaK122 system are desperately required.

In this study, we report growth of high-quality single crystals of $(\text{Ba}_{1-x}\text{K}_x)\text{Fe}_2\text{As}_2$ for all doping ranges ($0.22 \leq x \leq 1$) and report systematic study of their temperature-dependent resistivity and anisotropic upper critical fields. We found nearly doping independent resistivity value at high temperatures, which is in notable contrast to electron-doped BaCo122 [24] and isoelectron substituted BaP122 [16] materials. We found systematic evolution of the temperature dependent resistivity with doping and rapid decrease of residual resistivity towards $x = 1$. We also found that the slopes dH_{c2}/dT are proportional to T_c for both $H \parallel c$ and $H \parallel ab$ configurations. The anisotropy $\gamma \equiv H_{c2,ab}/H_{c2,c}$, increases from 2 to 4–5 with increasing K doping level. The doping dependence of

anisotropy ratio might be linked with change of the topology of the Fermi surface and the evolution of the superconducting gap.

II. EXPERIMENTAL

A. Crystal growth

We have previously described successful growth of high-quality single crystals of stoichiometric KFe_2As_2 at $T = 1157$ K using KAs flux [43]. One of the key elements of the growth technique was using a liquid-Sn sealing of alumina crucibles to suppress the evaporation of K and As. This technique allowed us to avoid use of quartz tubes in direct contact with K vapor and use of expensive sealed tantalum tubes. Analysis of the growth morphology in the case of KFe_2As_2 [43] lead us to conclude that the crystals nucleate on the surface of the melt and grow by the reaction on the top surface of the crystal with K and As in the vapor phase. We were able to promote this reaction by developing an inverted-temperature-gradient method with the colder zone at the top of the crucible, as shown in Fig. 1(a). A temperature gap of 20 K was set between the top zone and the bottom zone. This method yielded higher-quality crystals of KFe_2As_2 (as characterized by the residual resistivity ratio of up to 3000), than obtained in traditional flux method, as crystallization from the liquid top can expel impurity phases into the liquid during crystal growth.

This method works very well for the growth of heavily K-doped $(\text{Ba}_{1-x}\text{K}_x)\text{Fe}_2\text{As}_2$ single crystals. Small amount of Ba was added to the load with the ratio Ba:K:Fe:As= y :5:2:6 ($y = 0.1, 0.2, \text{ and } 0.3$) in the starting materials. The chemicals were weighed and loaded into an alumina crucible in a glove box under argon atmosphere. Because of use of higher soaking temperatures leading to higher vapor pressures Sn seal technique was not reliable enough, and we switched to tantalum tube sealing. The alumina crucibles were then

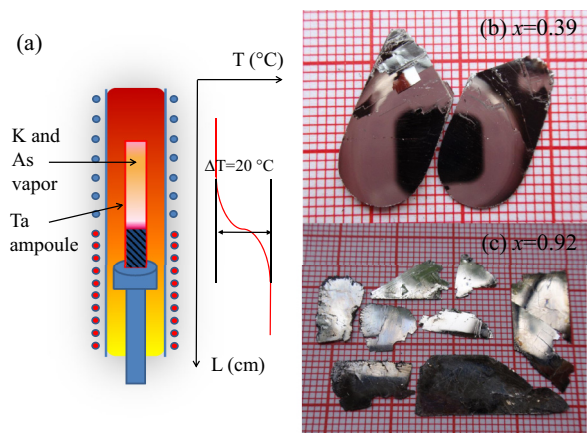


FIG. 1. (Color online) (a) Single crystals of $(\text{Ba}_{1-x}\text{K}_x)\text{Fe}_2\text{As}_2$ were grown in a vertical two-zone tube furnace, in which the temperature of the top zone during the growth was set 20 K lower than the temperature of the bottom zone. (b) Photograph of the as-grown single crystal with $x = 0.39$ cleaved along the ab plane, showing sample with in-plane dimensions up to 18×10 mm². The reflection of the camera can be seen in the mirrorlike surface. (c) Thin platelike crystal of heavily K-doped composition $x = 0.92$ with size up to 15×10 mm².

TABLE I. Growth conditions of $(\text{Ba}_{1-x}\text{K}_x)\text{Fe}_2\text{As}_2$ single crystals. Soaking temperature corresponds to the set temperature of bottom zone, with the top zone temperature 20 K lower than the bottom zone. Previously used methods and techniques of crystal growth of $(\text{Ba}_{1-x}\text{K}_x)\text{Fe}_2\text{As}_2$ are compared with inverted temperature gradient method in this study.

K content x in crystals	Starting mixtures Ba:K:Fe:As	Soaking temperature	Soaking time	Cooling rate	Previously used methods and techniques
0.22	$1 - x : x : 6 : 6$	1453 K	2 h	2 K/h to 1313 K	Sn flux method with double quartz sealing [34]. The crystals were separated from Sn flux in the centrifuge. Sn contamination.
0.34, 0.39, 0.47, and 0.53	$1 - x : 2x : 4 : 5$	1413 K	2 h	1 K/h to 1293 K	FeAs flux method with double quartz sealing [31]. Works well for $x \leq 0.40$. Potential As release if quartz ampoule is broken due to high soaking temperature.
0.55	$1 - x : 3x : 4 : 5$	1393 K	2 h	0.5 K/h to 1293 K	KAs flux method with commercial stainless steel container [33]. Works for overdoped crystals.
0.65, 0.80, and 0.82	$y : 4 : 2 : 5$ (Ba: y) $y = 0.2 \sim 0.3$	1273 K	6 h	4 K/h to 1173 K 1 K/h to 973 K	KAs and FeAs fluxes with liquid Sn sealing [43]. Potential As release depending on the amounts of K load and Sn for sealing.
0.90 and 0.92	$y : 4 : 2 : 5$ $y = 0.1$	1273 K	2 h	3 K/h to 1173 K 1 K/h to 973 K	
1	$y : 5 : 2 : 6$ $y = 0$	1193 K	1 h	4 K/h to 1093 K 1 K/h to 893 K	

sealed in a tantalum tube by arc welding. In Table I, we show the growth conditions of $\text{Ba}_{1-x}\text{K}_x\text{Fe}_2\text{As}_2$ single crystals. We started to grow heavily K-doped crystals by following the same procedure that worked well for the crystal growth of KFe_2As_2 . For $y = 0.1$, we obtained single crystals with K doping level at around $x = 0.90$ using soaking temperature of 1193 K. The actual compositions of the crystals were determined by wavelength dispersive x-ray spectroscopy (WDS) electron-probe microanalysis. For $y = 0.2$ and 0.3 , the single crystals obtained by cooling down from the soaking temperature of $T = 1193$ K display broad transitions, which suggests inhomogeneity of Ba and K distributions in the sample. We were able to improve sample quality by adjusting the composition of the starting load material and soaking temperatures, as shown in Table I. We found that increase of the soaking temperature to $T = 1273$ K helps growth of the samples with $x = 0.8$ and 0.9 with sharp superconducting transitions. The further increase of the soaking temperature up to 1323 K, leads to growth of the crystals showing multiple steps at the superconducting transition due to inhomogeneous K distribution. We found that higher soaking temperatures $1273 \text{ K} \leq T \leq 1323 \text{ K}$ and narrowed temperature window for crystal growth are similarly useful to grow the crystals within the doping range $0.6 < x < 0.9$ with sharp superconducting transition.

For the samples with K doping levels below $x = 0.55$, we turned to the FeAs flux method. The growth conditions can be found in Table I. For the crystals within the optimal doping range ($0.3 < x < 0.5$), the growth using conditions as shown in Table I yielded large and high-quality crystals with sharp transitions. Interestingly, to grow high-quality underdoped crystals, a further increase of the soaking temperature to 1453 K and fast cooling rate of 2 K/h are needed. A series of large and high-quality $(\text{Ba}_{1-x}\text{K}_x)\text{Fe}_2\text{As}_2$ single crystals ($0.22 \leq x \leq 1$) with sizes up to $18 \times 10 \times 1 \text{ mm}^3$, as shown in Fig. 1(b) for $x = 0.39$ and Fig. 1(c) for $x = 0.92$. In fact,

the size of $\text{Ba}_{1-x}\text{K}_x\text{Fe}_2\text{As}_2$ single crystals was only limited by the size of alumina crucibles used.

B. Sample characterization

XRD measurements were performed on a PANalytical MPD diffractometer using $\text{Co } K\alpha$ radiation. The $K\alpha_2$ radiation was removed with X'pert Highscore software. All BaK122 crystals are readily cleaved along the ab plane, as shown in Figs. 1(b) and 1(c). The XRD patterns of BaK122 single crystals with $0.22 \leq x \leq 1$ are shown in Fig. 2. The traces of impurity phases close to the baseline are indicated by the asterisks, they are most likely caused by the flux inclusions. Figure 2(b) shows systematic shift of the (008) peak towards the lower angles with increasing K content. The c -axis lattice parameter is estimated based on the (00 l) diffractions and displayed as a function of K content in Fig. 2(c); it changes linearly with x and its values match well the results on polycrystalline samples [37].

Magnetic susceptibility $\chi(T)$ was measured using PPMS Vibrating Sample Magnetometer (PPMS VSM, Quantum Design). Typical size of the single crystals used in magnetization measurements was $4 \times 3 \times 0.2 \text{ mm}^3$, and their mass was ~ 10 mg. In-plane resistivity ρ_a was measured in four-probe configuration using Physical Property Measurement System (PPMS, Quantum Design). Samples were cleaved into bars with typical dimensions $(1-2) \times (0.3-0.5) \times (0.02-0.05) \text{ mm}^3$. Electrical contacts were made by soldering Ag wires using pure tin [54,55] and had contact resistance typically in several $\mu\Omega$ range. Sample dimensions were measured using optical microscope with the accuracy of about 10%. Quantitative characterization of resistivity was made on a big array of samples of each composition.

Figure 3 shows the temperature-dependent magnetic susceptibility $\chi(T)$ for BaK122 single crystals with $0.22 \leq x \leq 1$. Sharp superconducting transitions ($\Delta T_c < 0.6$ K) in

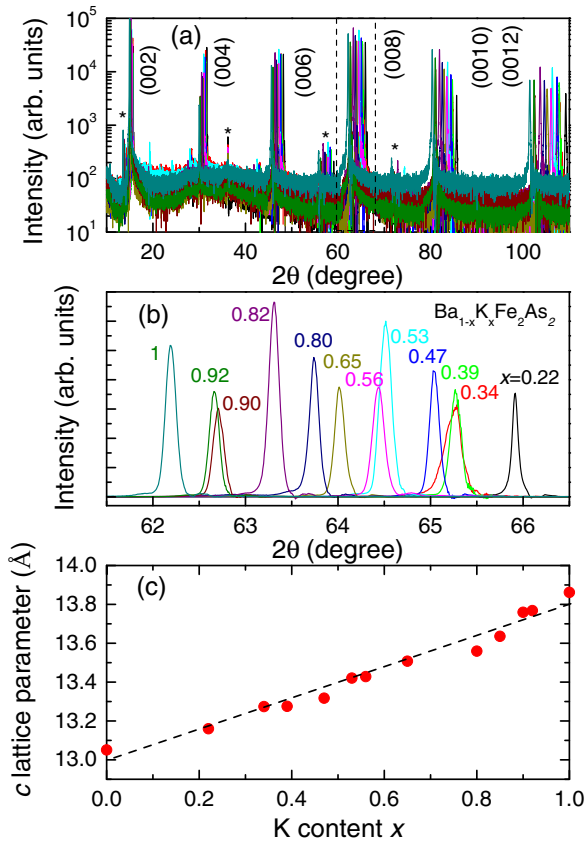


FIG. 2. (Color online) X-ray diffraction patterns of $(\text{Ba}_{1-x}\text{K}_x)\text{Fe}_2\text{As}_2$ $0.22 \leq x \leq 1$ single crystals. The logarithmic plot reveals small amount of impurity phases indicated by the asterisks, which could result from the FeAs and KAs flux inclusions. (b) The (008) peak, seen in $61^\circ < 2\theta < 67^\circ$ range, systematically shifts with increasing K doping level towards the low angles. (c) The c lattice parameter changes linearly with the K content x . The dashed line is guide for eyes.

magnetic susceptibility curves show high quality of crystals with $x = 0.34, 0.39, 0.47, 0.53, 0.55$, and 1 . The transition width ΔT_c was defined using 90% and 10% drop in $\chi(T)$ of the full diamagnetic transition as the criterion. The samples with $x = 0.82, 0.90$, and 0.92 have $\Delta T_c < 1$ K. However, the samples with $x = 0.65$ and 0.80 have large ΔT_c of 3 K and 5 K, respectively. As we mentioned in the Experimental section, we shifted the temperature windows and adjusted the setting load composition and materials to improve the sample quality and obtain sharper transitions.

Using T_c from magnetic susceptibility data of top panel of Fig. 3 and x values as obtained in WDS analysis, we constructed the doping phase diagram, as shown in bottom panel of Fig. 3. For reference, we show the diagram as determined from measurements on high-quality polycrystalline materials [35–37]. The two studies are in good agreement.

We do not see any indications of the phase separation in our underdoped samples $x = 0.22$. Previous study of underdoped BaK122 samples grown from Sn flux with $x = 0.28$ found regions of antiferromagnetically (AF) ordered phase with size of 65 nm coexisting with nonmagnetic superconducting regions [56]. Later study using three-dimensional (3D) atom

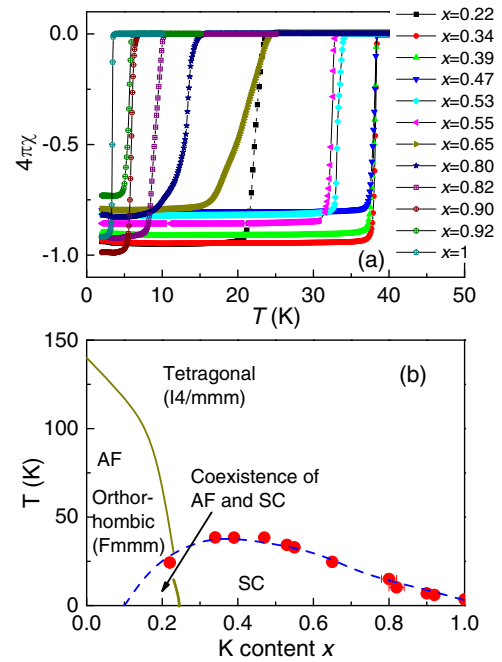


FIG. 3. (Color online) (a) Temperature dependence of the magnetic susceptibility $\chi(T)$ of $(\text{Ba}_{1-x}\text{K}_x)\text{Fe}_2\text{As}_2$ $0.22 \leq x \leq 1$ single crystals. Bulk superconducting transition temperature T_c was determined from the onset point of the rapid drop of $\chi(T)$. (b) Doping phase diagram of $(\text{Ba}_{1-x}\text{K}_x)\text{Fe}_2\text{As}_2$ as determined from magnetization measurements on single crystals $0.22 \leq x \leq 1$. The superconducting transition temperature (red solid dots), $T_c(x)$, matches well that obtained on polycrystalline samples (blue dashes) [35–37]. Solid line shows boundary of orthorhombic/antiferromagnetic phase from neutron scattering study on polycrystals [35–37].

probe tomography revealed that the separation is caused by inhomogeneous distributions of Ba and K elements [57], with a tendency for Ba and K atoms to form clusters. Thus we conclude that this problem is not characteristic of the growth technique we use.

We do see, however, that strong inhomogeneity occurs during crystal growth of overdoped crystals ($0.65 < x < 0.8$). There is no intrinsic phase separation revealed for polycrystalline samples in this doping range. In our samples, we do not see macroscopic inhomogeneity in WDS measurements with spatial resolution of about $1 \mu\text{m}$. On the other hand, phase separation on a finer scale was found in two STM studies. Imaging of vortex lattice in single crystals of optimally doped BaK122 $x = 0.40$ [58] found regular lattice, but a short-range order (vortex glass phase) in single crystals of SrK122 $x = 0.25$ [59]. Song *et al.* suggested that mismatch between the size of the dopant K atom and of the host atoms Ba and Sr, $\text{Ba}^{2+}/\text{K}^+$ and $\text{Sr}^{2+}/\text{K}^+$, respectively, causes dopant clustering and electronic inhomogeneity [59]. This idea, however, does not provide any explanation why the distribution is more homogeneous for samples close to optimal doping, whereas dopant clustering becomes serious within the doping range $0.65 \leq x \leq 0.8$. From the perspective of the crystal growth, high growth rates should be helpful to suppress segregation, and higher soaking temperatures should help to mix the dopant in the liquid melt. Because of this segregation

problem, it is important to optimize growth conditions for overdoped single crystals. Finally, we would like to point out that in our high-quality $(\text{Ba}_{1-x}\text{K}_x)\text{Fe}_2\text{As}_2$ single crystals, c lattice parameter monotonically increases with increasing K doping level, which suggests that the evolution of lattice parameters is not affected by possible clustering.

III. RESULTS AND DISCUSSION

A. Doping evolution of the temperature-dependent resistivity

Temperature dependent in-plane resistivity $\rho(T)$ of the samples with $x = 0.22$ to 1.0 is shown in Fig. 4. The data are presented using normalized $\rho(T)/\rho(300\text{ K})$ plots and offset to avoid overlapping. The doping evolution of the actual resistivity values $\rho(300\text{ K})$ shows significant scatter due to uncertainty of the geometric factors, which are strongly affected by hidden cracks in micacious crystals of iron pnictides [22,26]. Of note though that within statistical error, the resistivity $\rho(300\text{ K})$ remains constant over the whole compositional range from heavily underdoped samples with $x = 0.22$ to heavily overdoped $x = 1.0$, which is distinctly different from electron doped BaCo122 [24,60] and isoelectron substituted BaP122 [16], in which $\rho(300\text{ K})$ decreases notably with doping. The first look at the temperature-dependent resistivity also does not show significant doping evolution. For all doping levels the $\rho(T)$ curves show a broad crossover starting above 100 K and ending at around 200 K. The onset of this feature most clearly reveals itself as a maximum in

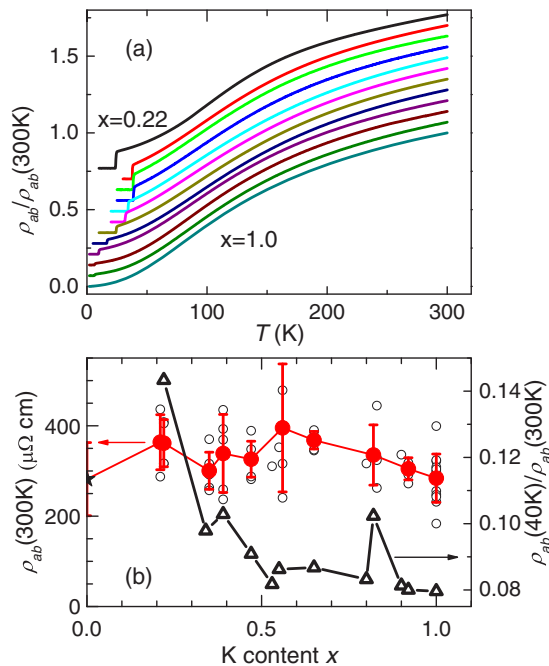


FIG. 4. (Color online) (a) Temperature dependence of in-plane resistivity in single crystals of $(\text{Ba}_{1-x}\text{K}_x)\text{Fe}_2\text{As}_2$ (top to bottom $x = 0.22, 0.34, 0.39, 0.47, 0.53, 0.55, 0.65, 0.80, 0.82, 0.90, 0.92, 1.0$). The data are presented using normalized $\rho(T)/\rho(300\text{ K})$ plot and offset for clarity. (b) (right scale) Doping evolution of the $\rho(40\text{ K})/\rho(300\text{ K})$ and (left scale) of the room-temperature resistivity $\rho(300\text{ K})$, open dots are data for individual samples, solid dots with error bars show statistical average and standard deviation.

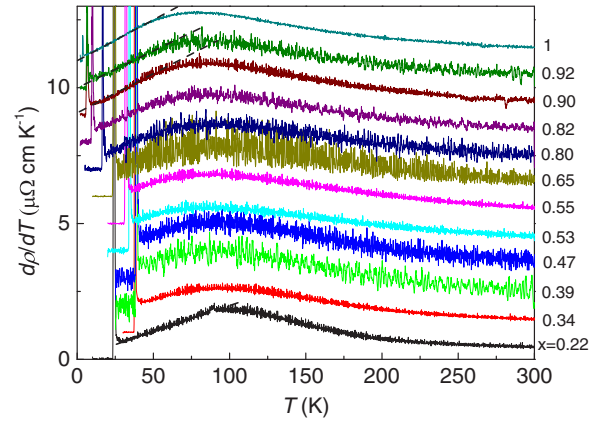


FIG. 5. (Color online) Doping evolution of the temperature-dependent derivative of in-plane resistivity, $d\rho_a(T)/dT$, in single crystals of $(\text{Ba}_{1-x}\text{K}_x)\text{Fe}_2\text{As}_2$ $0.22 \leq x \leq 1$. The data are offset to avoid overlapping.

the temperature-dependent resistivity derivative, see Fig. 5. The origin of the feature was discussed in terms of multi-band character of conductivity in which one of the bands has strongly temperature dependent contribution, while the other has nearly temperature independent conductivity [38], as contribution from phonon-assisted scattering between two Fermi-surface sheets [45] and as a feature associated with pseudogap, as suggested by its correlation with the maximum of the interplane transport $\rho_c(T)$ in underdoped compositions [24,25,30]. The position of the crossover does not change with doping, and since the Fermi surface topology reveals quite significant changes [61], the explanation of the maximum in term of special features of band structure [38,45] is very unlikely.

At temperatures lower than 100 K, however, temperature-dependent resistivity shows some evolution. Because of high temperature of the superconducting transition, we cannot make correct analysis of the functional form of $\rho(T)$ in the $T \rightarrow 0$ limit over the whole dome. However, for the sake of comparison, we fitted the curves in a narrow range from 40 to 60 K, which was fixed for all compositions. These fits were done two ways. The first approach was using second order polynomial function, $\rho(T)/\rho(300\text{ K}) = \alpha_0 + \alpha_1 T + \alpha_2 T^2$, similar to the fit used by Doiron-Leyraud *et al.* [62] for electron-doped BaCo122. In the top panel of Fig. 6, we show the fits over the range 40 to 60 K for $\rho(T)$ curves for representative doping levels, three bottom panels show doping evolution of the fit parameters α_0 , α_1 , and α_2 . This analysis reveals clearly that the dependence has highest linear contribution at $x = 0.35$ and 0.39, and that the T^2 contribution is minimum at $x = 0.39$, coinciding with maximum T_c position but away from the doping border of the antiferromagnetic state at $x = 0.26$.

The second approach was fitting the data using a power-law function, $\rho/\rho(300\text{ K}) = \rho_0 + AT^n$, as shown for selected compositions in Fig. 7. This approach is similar to the approach used by Shen *et al.* [29], however, in their case the fitting range was extending to 80 K. For the sake of comparison, we did power-law analysis for the temperature ranges 40 to 70 K and 40 to 80 K, and from above T_c to 60 K. The results of these

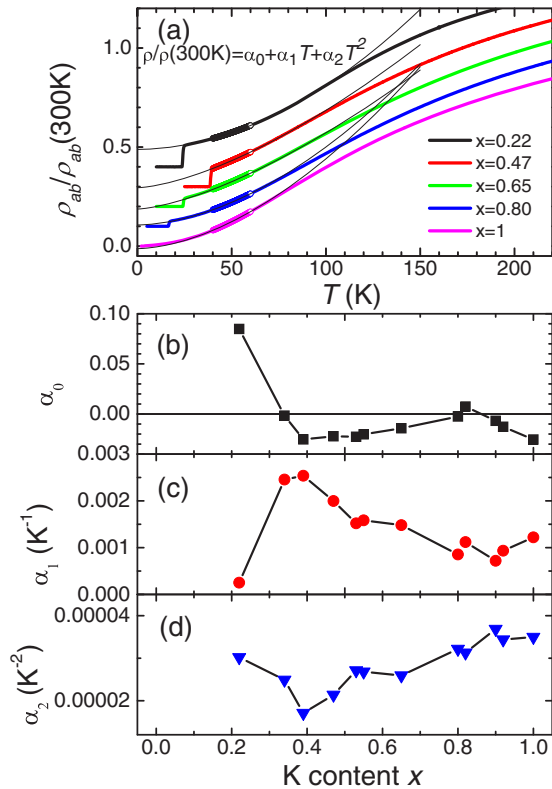


FIG. 6. (Color online) (a) (Top) Fixed 40 to 60-K range fit of the resistivity curves using second order polynomial $\rho/\rho(300\text{ K}) = \alpha_0 + \alpha_1 T + \alpha_2 T^2$, shown for selected dopings $x = 0.22, 0.47, 0.65, 0.8, 1$. The data are offset to avoid overlapping. Three panels at the bottom show doping evolution of the fit parameters α_0 (b), α_1 (c), and α_2 (d).

fits are shown in the bottom panel of Fig. 7. It can be seen that all ways of analysis find largest deviations from Fermi-liquid T^2 dependence at $x = 0.39$, which corresponds to a leading edge of maximum T_c plateau of the $T_c(x)$ dome. Since $T_c(x)$ function is nearly flat in 0.34 to 0.56 range, while both T -linear contribution in the polynomial analysis, Fig. 6(c), and power-law exponent n peak at $x = 0.39$, we conclude that T_c and the amplitude of T -linear contribution do not scale in BaK122, contrary to BaCo122 [12]. Another interesting point is that exponent n , we observe in sample $x = 0.39$ is close to 1.5. This is notably higher than the lowest exponent $n = 1.1$ found in previous study [29]. To further check the link between T -linear contribution and maximum T_c , further studies in high magnetic fields may be necessary.

An interesting feature of these fits is that the residual resistivity takes negative values for most of the compositions. This fact is suggestive that at lower temperatures the $\rho(T)$ curves should develop significant positive curvature, as is in fact observed for heavier doped compositions, in which broader temperature range can be studied. It also suggests that most of our samples have quite high residual resistivity ratio in $T \rightarrow 0$ limit.

On the other hand, the T^2 coefficient as determined from the polynomial fit for the range 40 to 60 K gradually increases towards $x = 1$. Since T_c drops significantly in this range, we are able to make an analysis at lower temperatures. In Fig. 8,

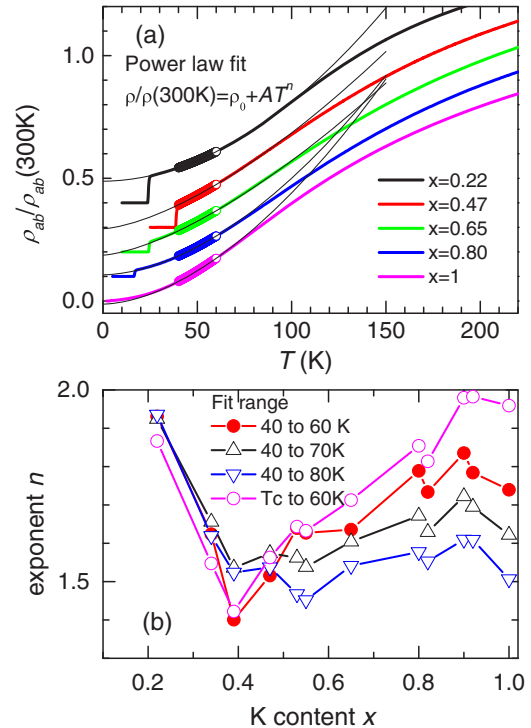


FIG. 7. (Color online) (Top) Fixed 40 to 60-K range fit of the resistivity curves using power-law function $\rho/\rho(300\text{ K}) = \rho_0 + AT^n$, shown for selected dopings $x = 0.22, 0.47, 0.65, 0.8, 1$. The data are offset to avoid overlapping. Bottom panel shows evolution of the power-law exponent n with doping for fits over four different temperature ranges, 40 to 60 K as shown in top panel (red solid circles), 40 to 70 K (black up-triangles), 40 to 80 K ((blue down-triangles) and T_c to 60 K (magenta open circles).

we plot $\rho(T)$ data for all samples using a T^2 plot, bottom panel shows expanded view for heavily overdoped samples. When plotted this way, the plots become linear right above T_c , and the slopes of the curves do not show any noticeable doping evolution beyond error bars. This observation suggests that for all doping levels there is significant and noncritical T^2 contribution, and indeed several contributions to conductivity are needed for correct account of its doping evolution.

B. Anisotropic upper critical fields

The anisotropy of the upper critical field $\gamma_H \equiv \frac{H_{c2ab}}{H_{c2c}}$ presents important information about the anisotropy of the electrical resistivity, $\gamma_\rho \equiv \frac{\rho_c}{\rho_a}$. In a temperature range, close to zero-field T_c , the anisotropy of H_{c2} for s -wave superconductors in the clean limit can be written as $\gamma_H^2 = \langle v_a^2 \rangle / \langle v_c^2 \rangle$ [63], or roughly $\gamma_H \sim v_a / v_c$, where v_a and v_c are Fermi velocities for a and c directions, respectively. Assuming that the mean-free path is isotropic, the anisotropy of resistivity $\rho_c / \rho_a = \sigma_a / \sigma_c \sim N_a D_a / N_c D_c$, where N s are densities of states and D s are diffusivities, which are both proportional to v . Hence $\gamma_\rho = \rho_c / \rho_a = (v_a / v_c)^2$, and $\gamma_H^2 \sim \gamma_\rho$. In the dirty limit near T_c , $H_{c2} \sim 1 / \xi_{\text{dirty}}^2 \sim 1 / D \sim 1 / v$ and again $\gamma_H \sim v_a / v_c$, unless the scattering itself is anisotropic. Hence, we again have

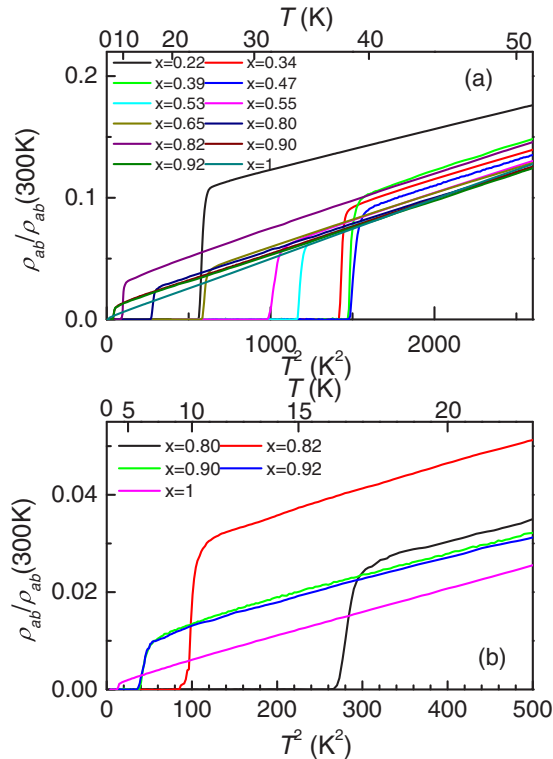


FIG. 8. (Color online) (Top) Normalized resistivity curves $\rho/\rho(300\text{ K})$ plotted vs T^2 for all doping levels studied, $x = 0.22, 0.34, 0.39, 0.47, 0.53, 0.55, 0.65, 0.80, 0.82, 0.90, 0.92, 1.0$. Bottom panel shows data over narrower temperature range in heavily overdoped compositions $x = 0.80, 0.82, 0.90, 0.92, 1.0$. The data does not show any significant dependence of the slope (proportional to T^2 coefficient α_2) even at low temperatures.

$\gamma_H^2 \sim \gamma_\rho$. Although approximate, this relation was verified semi-quantitatively in the optimally doped BaCo122 [22] and in KFe_2As_2 [40]. The angular dependent $H_{c2}(\Theta)$ was also studied systematically in BaK122 with $x = 0.92$ [53], in which the authors found strong deviations from $\cos(\Theta)$ dependence expected in the orbital limit [64]. Scattered in x measurements of γ_H were undertaken on samples close to optimal doping grown from Sn flux [34,45,46,65] and from FeAs flux [47,66]. Here, we study evolution of the $\gamma_H(x)$ in BaK122 from resistive H_{c2} measurements.

In Fig. 9, we show zoom of the $\rho(T)$ curve in the vicinity of the superconducting transition in sample with $x = 0.39$. Here, we show how we defined different criteria used to determine $T_c(H)$ dependence. We analyzed resistivity data by linear extrapolation of $\rho(T)$ curves at the transition and above the transition. The onset $T_{c,\text{onset}}$ of the transition is defined at the crossing point of these linear fits. The offset T_c corresponds to the crossing point of the steep transition line with $\rho = 0$ line.

In Fig. 10, we show resistivity data taken in magnetic fields parallel to c axis (top panels), parallel to the conducting ab plane (middle panels) and temperature dependent $H_{c2}(T)$ for two field orientations determined using onset and offset criteria. The data are shown for BaK122 compositions with $x = 0.22$ (a), 0.34 (b), 0.39 (c), and 0.47 (d). Similar data for slightly to moderately overdoped compositions $x = 0.53$

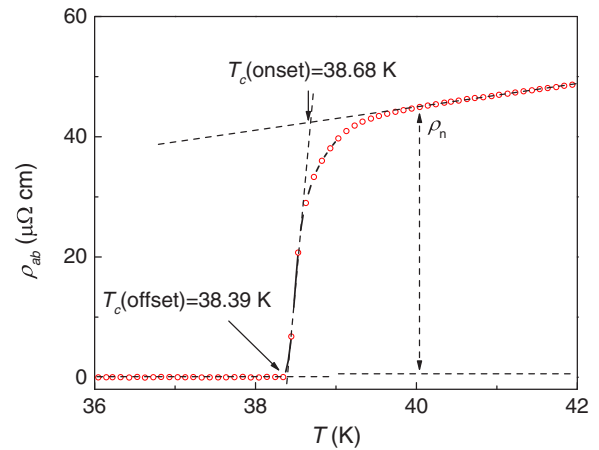


FIG. 9. (Color online) Temperature-dependent resistivity in single crystal of $(\text{Ba}_{1-x}\text{K}_x)\text{Fe}_2\text{As}_2$ with $x = 0.39$ in the vicinity of the superconducting transition. The onset $T_{c,\text{onset}}$ of the transition is defined at the crossing point of the linear fits of the $\rho(T)$ in the normal state above T_c and at the sharp transition slope. The offset T_c corresponds to the extrapolation of the steep transition slope to zero resistance.

(a), 0.55 (b), 0.65 (c), 0.80 (d) are shown in Fig. 11, and for strongly overdoped compositions $x = 0.82$ (a), 0.90 (b), 0.92 (c), and 1.0 (d) in Fig. 12.

For the samples with $x = 0.22, 0.34, 0.39, 0.47, 0.53, 0.55$, the $H_{c2}(T)$ curves show positive curvature close to $T_c(0)$ for lowest fields below $H = 1$ T. Going further below $T_c(0)$, the $H_{c2}(T)$ gets practically T linear. This is exactly the range which we use for determination of the dH_{c2}/dT slope and evaluation of $H_{c2}(0)$ as $H_{c2}(0) = -0.70T_c(0)dH_{c2}/dT$ (as shown in Fig. 13). For the heavily overdoped samples $x = 0.80, 0.82, 0.90, 0.92$, and 1, the $H_{c2}(T)$ curves in configuration $H \parallel ab$ show a clear decrease of slope on cooling with a tendency to saturation, whereas for $H \parallel c$ the curves remain linear. Therefore the linear fit only can be applied to the data close to T_c , as shown in the bottom panels of Fig. 12. The saturation in $H \parallel ab$ reflects paramagnetic Pauli limiting [67]. Similar saturation behavior is seen in underdoped samples [46].

In Fig. 13(b), we summarize the doping evolution of the slope of the temperature dependent upper critical field for field orientations along c axis (open black circles) and along the plane (closed red circles) (middle panel). In the Werthamer-Helfand-Hohenberg (WHH) theory [68] of the upper critical field for the orbital limiting mechanism, $H_{c2}(0) = -0.7T_c(0)dH_{c2}/dT$. In Fig. 13(c), we plot $H_{c2}(0)$ estimated using WHH formula as $-0.7T_c(0)dH_{c2}/dT$. Note the huge values of $H_{c2,c} > 100$ T for compositions close to optimal doping. Interesting, the $H_{c2,c}(x)$ and especially $H_{c2,ab}(x)$ dependencies peak at 0.39 and are much sharper than $T_c(x)$ dependence.

C. Doping evolution of the anisotropy parameter γ

In the bottom panel of Fig. 13, we plot doping evolution of the anisotropy of the upper critical field $\gamma(x)$. It can be seen that γ increases approximately two times, from 2 to 4 to

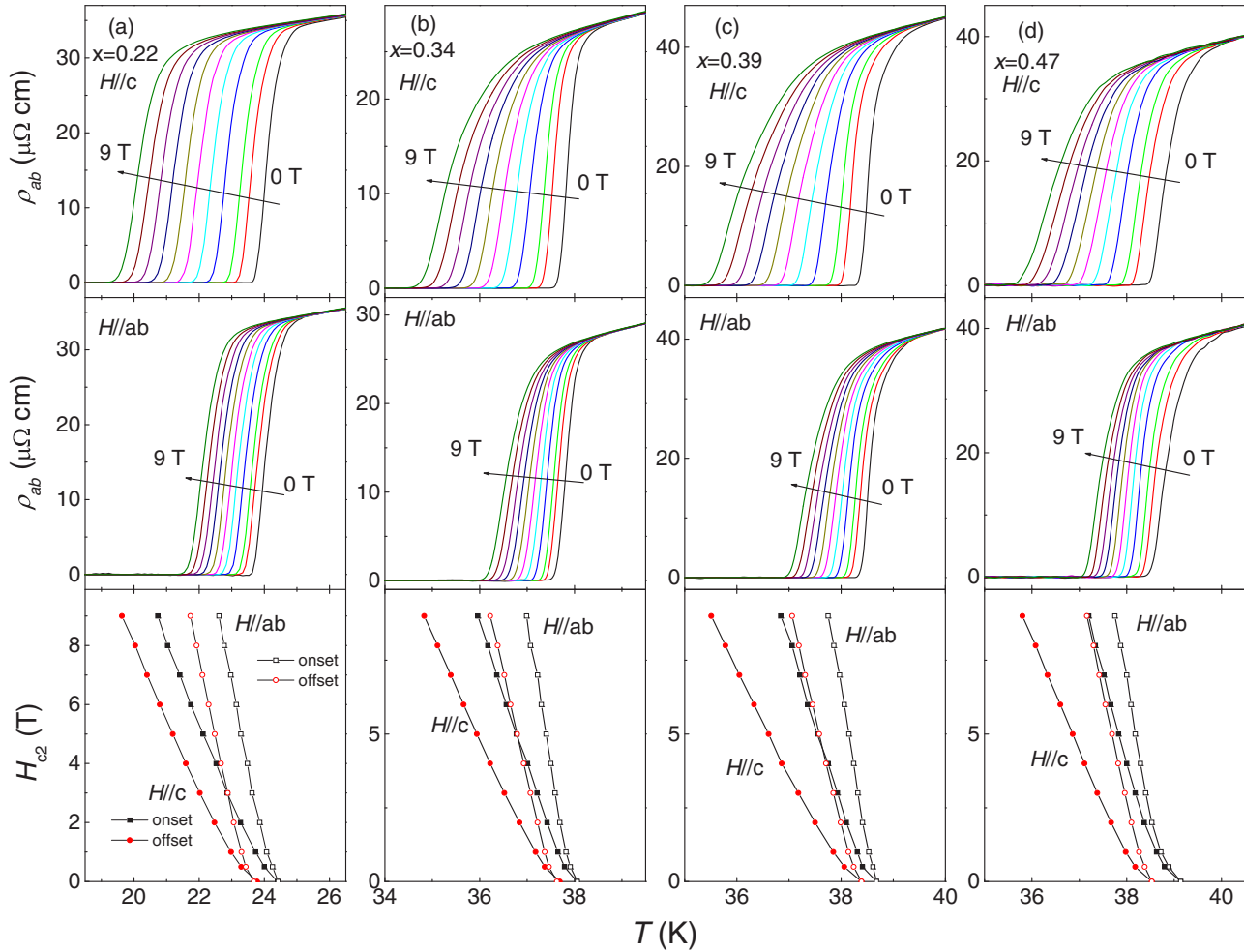


FIG. 10. (Color online) Temperature dependence of in-plane resistivity in single crystals of $(\text{Ba}_{1-x}\text{K}_x)\text{Fe}_2\text{As}_2$ with $x = 0.22$ (a), 0.34 (b), 0.39 (c), and 0.47 (d) in magnetic fields $H \parallel c$ (top panels) and $H \parallel ab$ (middle panel) with magnetic fields (right to left) $0, 0.5, 1, 2, 3, \dots, 9$ T. Bottom panels show $H_{c2}(T)$ for two field orientations $H \parallel c$ (solid symbols) and $H \parallel ab$ (open symbols) as determined using onset (black squares) and offset (red circles) resistive transition criteria, see Fig. 9.

5 (depending on criterion) with increasing K doping levels. The increase starts in the heavily overdoped compositions $x > 0.82$, not far from the point where the Fermi surface topology change was found in angle-resolved photoelectron spectroscopy (ARPES) studies [61] and where the magnetism of the compounds changes according to neutron scattering [69,70] and NMR [71] studies. According to ARPES studies, the electron sheet of the Fermi surface transforms to four tiny cylinders. Since electron sheets are most warped [22], it is natural to expect an anisotropy increase close to $x = 1$ end of the doping phase diagram, in line with the upper critical anisotropy increase with x .

Several previous studies of H_{c2} anisotropy for selected x close to optimal doping in BaK compounds were performed in high magnetic fields up to 60 T in samples with $T_c = 28.2$ K ($x = 0.4$) [46], $T_c = 32$ K ($x = 0.45$) [65], and $T_c = 38.5$ K ($x = 0.32$) [45]. They found anisotropy decreasing on cooling, which was presumably caused by contribution of paramagnetic effect for $H_{c2,ab}$.

Similar to high-field studies in single crystals of other iron-based superconductors BaCo122 $x = 0.14$ [45,72],

$\text{NdFeAsO}_{0.7}\text{F}_{0.3}$ [73], LiFeAs [74], and $\text{FeTe}_{0.6}\text{Se}_{0.4}$ [75,76], we find rough linear increase of the $H_{c2,c}(T)$, but concave dependence with a tendency for saturation for $H_{c2,ab}$. For all compounds of iron based superconductors, the anisotropy ratio γ at $T_c(0)$ is in the range 2 to 5, similar to our finding in BaK122, with $\text{Ca}_{10}(\text{Pt}_3\text{As}_8)((\text{Fe}_{1-x}\text{Pt}_x)_2\text{As}_2)_5$ with $x = 0.09$ [77], $\text{SmFeAsO}_{0.85}\text{F}_{0.15}$ [78] and $\text{LaFe}_{0.92}\text{Co}_{0.08}\text{AsO}$ [79] being exceptions, with $\gamma \approx 7$ to 8.

Additional contribution to the doping evolution of the anisotropy of the upper critical field can come from the evolution of the superconducting gap structure [80]. Initial high-resolution ARPES studies on optimally doped samples with $x = 0.4$ revealed a superconducting large gap ($\Delta \sim 12$ meV) on the two small holelike and electronlike Fermi surface sheets, and a small gap (~ 6 meV) on the large holelike Fermi surface [81]. In heavily overdoped KFe_2As_2 , the Fermi surface around the Brillouin-zone center is qualitatively similar to that of composition with $x = 0.4$, but the two electron pockets are absent due to an excess of the hole doping [82]. An ARPES study over a wide doping range of BaK122 discovered that the gap size of the outer hole Fermi surface sheet around the

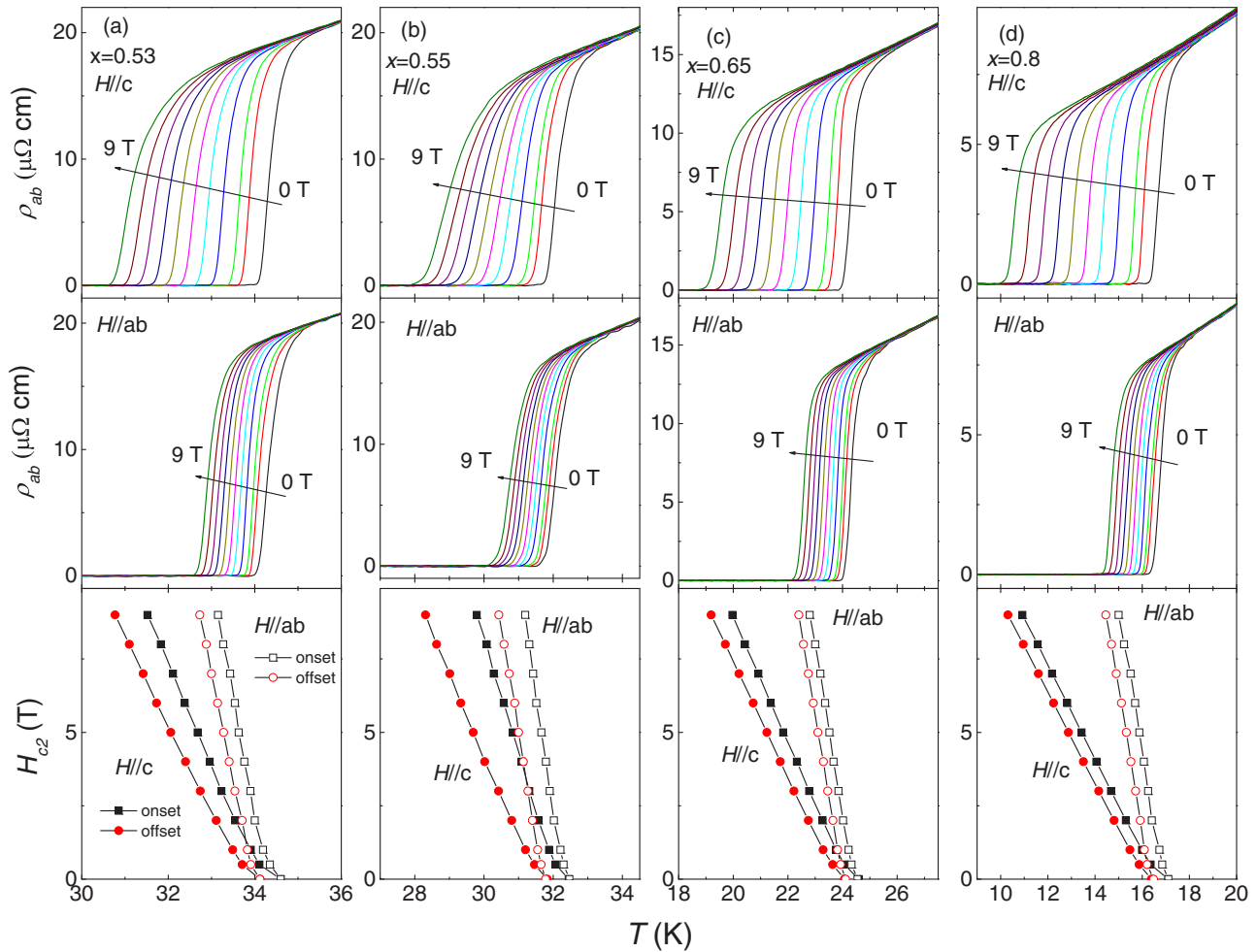


FIG. 11. (Color online) Temperature dependence of in-plane resistivity in single crystals of $(\text{Ba}_{1-x}\text{K}_x)\text{Fe}_2\text{As}_2$ with $x = 0.53$ (a), 0.55 (b), 0.65 (c), and 0.80 (d) in magnetic fields $H \parallel c$ (top panels) and $H \parallel ab$ (middle panel) with magnetic fields (right to left) $0, 0.5, 1, 2, 3, \dots, 9$ T. Bottom panels show $H_{c2}(T)$ for two field orientations $H \parallel c$ (solid symbols) and $H \parallel ab$ (open symbols) as determined using onset (black squares) and offset (red circles) resistive transition criteria, see Fig. 9.

Brillouin zone center shows an abrupt drop with overdoping (for $x \geq 0.6$), while the gaps on the inner and middle sheets roughly scale with T_c [83].

D. Linear relation between $H_{c2}(T)$ slope and T_c

The high values of the critical fields in iron pnictides are determined by their short coherence lengths in 1- to 3-nm range [84], due to their high T_c and low Fermi velocities, v , with $\xi \sim \hbar v / 2\pi k_B T_c$. Discussing the reasons for remarkable proportionality of the slopes of dH_{c2}/dT to T_c for both field directions shown in Fig. 14, we recall that in *clean* isotropic s-wave materials,

$$H_{c2} = -\frac{\phi_0(1 - T/T_c)}{2\pi\xi_0^2}, \quad \xi_0 \sim \frac{\hbar v}{\Delta_0} \propto \frac{v}{T_c}, \quad (1)$$

so that the slope $H'_{c2} \propto T_c$. For the dirty case, H'_{c2} is T_c independent; indeed,

$$H_{c2} \propto \frac{1 - T/T_c}{\xi_0 \ell}, \quad (2)$$

where ℓ is the T independent mean-free path.

We should mention that a strong pair breaking could be another reason for $dH_{c2}/dT \propto T_c$. For a gapless uniaxial material, the slope of the upper critical field along the c direction near T_c is given by [85]

$$\frac{dH_{c2,c}}{dT} = -\frac{4\pi\phi_0 k_B^2}{3\hbar^2 \langle \Omega^2 v_{ab}^2 \rangle} T_c. \quad (3)$$

Here, $\Omega(\mathbf{k}_f)$ describes the anisotropy of the order parameter and is assumed to have a zero Fermi surface average, $\langle \Omega \rangle = 0$, which is the case for the d -wave or, approximately, for the s^\pm symmetry.

In our view, the first reason, i.e., the long mean free path, is a probable cause for $dH_{c2}/dT \propto T_c$. Studies of thermal conductivity [86] and London penetration depth [87] at optimal doping suggest full gap, which is inconsistent with the idea of gapless superconductivity. In Fig. 14, we verify linear relation for BaK122 over a broad doping (and as a consequence T_c) range, using onset (a) and offset (b) criteria. The relation indeed holds very well, especially for $H \parallel c$ configuration where the $H_{c2,0}(x)$ curves extrapolate to zero on $T_c \rightarrow 0$. This suggests that there is no gross change in the Fermi velocity over the whole doping range. The linear relation between the slope

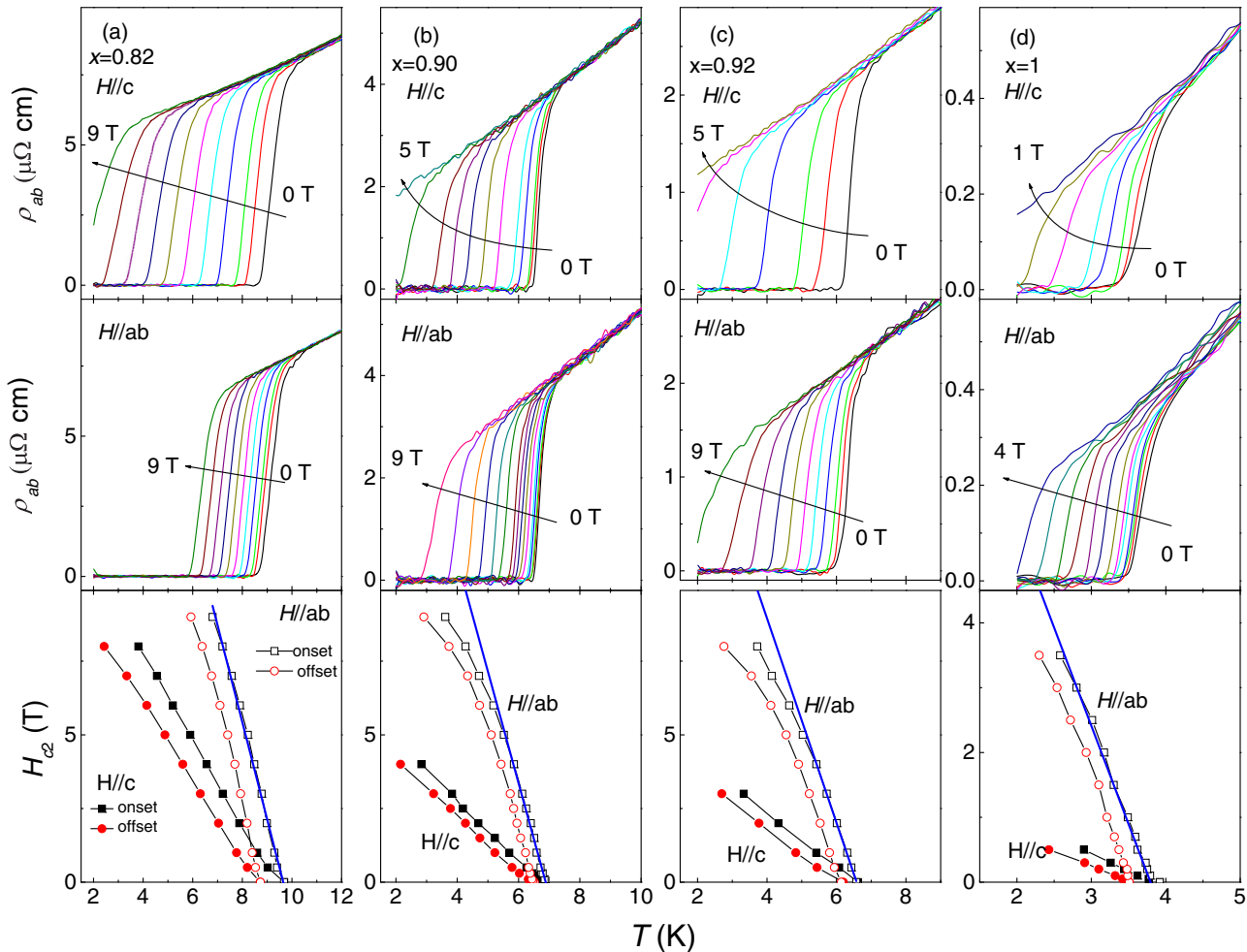


FIG. 12. (Color online) (Top panels) Temperature dependence of in-plane resistivity in single crystals of $(\text{Ba}_{1-x}\text{K}_x)\text{Fe}_2\text{As}_2$ with $x = 0.82$ (a) (right to left 0, 0.5, 1, 2, 3, ..., 9 T), 0.90 (b) (right to left 0, 0.05, 0.1, 0.3, 0.5, 1, 1.5, 2, 2.5, 3, 4, 5 T), 0.92 (c) (right to left 0, 0.5, 1, 2, ..., 5 T), and 1 (d) (0, 0.05, 0.1, 0.2, 0.3, 0.5, 0.7, 1 T) in magnetic fields $H \parallel c$. Middle panels show the data for $H \parallel ab$ (a), $x = 0.82$, right to left 0, 0.5, 1, 2, 3, ..., 9 T, (b) $x = 0.90$, field values right to left 0, 0.05, 0.1, 0.3, 0.5, 1, 1.5, 2, 2.5, 3, 4, ..., 9 T, (c) $x = 0.92$ right to left 0, 0.5, 1, 2, 3, ..., 9 T and (d) $x = 1$ magnetic fields 0, 0.1, 0.2, 0.3, 0.5, 0.7, 1, 1.5, 2, 2.5, 3, 3.5, 4 T. Bottom panels show $H_{c2}(T)$ for two field orientations as determined using onset (squares) and offset (circles) of resistive transition criteria, see Fig. 9. Thick blue lines show linear fits of the data for fields close to zero-field $T_c(0)$ neglecting slight upturn in the lowest fields in the bottom panels.

of the H_{c2} line and T_c is grossly violated in KFe_2As_2 when T_c is controlled by disorder: here the slope was found to be independent of T_c [43], despite the sample being clearly in the clean limit. For $H \parallel ab$, the $H_{c2,0}(x)$ curve is also close to linear, but does not extrapolate to zero on $T_c \rightarrow 0$. This deviation may be suggestive that Fermi velocity for transport along the c axis is strongly decreasing in BaK compositions with lowest T_c close to $x = 1$.

Another way to check the linear relation between the slope of the upper critical field and T_c is to plot their ratio, as shown in the bottom panel (c) of Fig. 14. Plotting data this way reveals one difficult to recognize feature. The data for $H \parallel c$ indeed show constant and doping independent ratio $\frac{dH_{c2}/dT}{T_c}$. The ratio for $H \parallel ab$ remains constant for most of the phase diagram and then increases rapidly for $x > 0.8$, showing that the increase of the anisotropy in this range is caused by decrease of the Fermi velocity, as one would expect for more anisotropic materials. The robustness of the linear relation between the slope and the

T_c suggest that BaK122 for all doping levels can be treated in clean limit, reflecting on very short coherence lengths and long mean free paths, as mentioned above.

IV. CONCLUSIONS

Using an inverted temperature gradient method we were able to grow large and high-quality single crystals of $(\text{Ba}_{1-x}\text{K}_x)\text{Fe}_2\text{As}_2$ with doping range spanning from underdoped to heavily overdoped compositions ($0.22 \leq x \leq 1$). We show that high vapor pressure of K and As elements at the soaking temperature is an important factor in the growth of single crystals of BaK122. When setting the top zone as the cold zone, on cooling the nucleation starts from the surface layer of the liquid melt. It is also assisted by the vapor growth, because surface layer also saturates first due to the evaporation of K and As. The crystallization processes from the top of a liquid melt helps to expel impurity phases

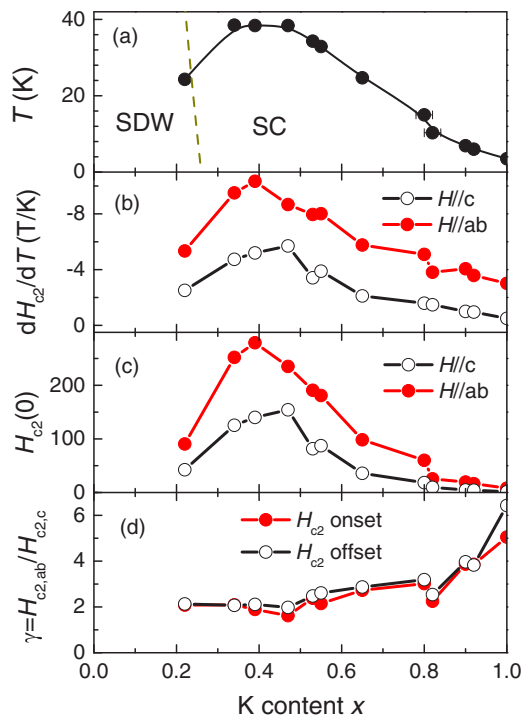


FIG. 13. (Color online) Doping evolution of the slope of $H_{c2}(T)$ curves close to zero-field $T_c(0)$, $dH_{c2}(T)/dT$ (b), of the extrapolated $H_{c2}(0) = -0.70T_c(0)dH_{c2}/dT$ (c), and of anisotropy of the upper critical field $\gamma \equiv H_{c2,ab}/H_{c2,c}$ (d), shown in comparison with doping evolution of the superconducting transition temperature $T_c(x)$ (a).

during, compared to the growth inside the flux. For the whole doping range $0.22 \leq x \leq 1$, we harvested large crystals with in-plane size up to $18 \times 10 \text{ mm}^2$. The crystals show very sharp superconducting transitions (less than 1 K) in dc magnetic susceptibility measurements for the optimal doping, $0.34 \leq x \leq 0.55$, and extremely overdoping, $0.82 \leq x \leq 1$, regimes. Relatively broad transitions are observed in the samples $x = 0.65$ and 0.80 , due to a broader distribution of Ba and K atoms and a tendency to K clustering in the lattice [57,59].

In-plane electrical resistivity shows systematic evolution with doping. It perfectly follows the T^2 dependence in the overdoped compositions with a doping-independent slope over the range 0.80 to 1 . Close to optimal doping, the dependence deviates from the pure T^2 functional form and can be described either as a sum of T linear and T^2 contributions, similar to

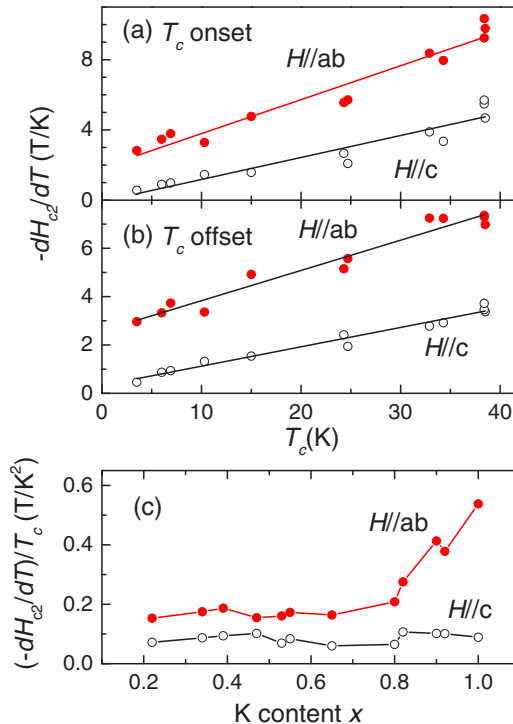


FIG. 14. (Color online) Dependence of the slope of the upper critical field, $dH_{c2}(T)/dT$ at T_c , on the superconducting transition temperature T_c for magnetic field parallel to tetragonal c axis (open black circles) and parallel to the ab plane (solid red circles) using onset (top panel) and offset (bottom panel) criteria.

electron-doped materials [62], or using a power-law function with exponent $n \approx 1.5$.

The anisotropy of the upper critical field shows a rapid change in the heavily overdoped regime, concomitant with Fermi surface reconstruction. The slope of the $H_{c2}(T)$ curves scales with the zero-field T_c of the samples, suggesting a nearly doping-independent Fermi velocity.

ACKNOWLEDGMENTS

This work was supported by the U.S. Department of Energy (DOE), Office of Science, Basic Energy Sciences, Materials Science and Engineering Division. The research was performed at the Ames Laboratory, which is operated for the US DOE by Iowa State University under contract DE-AC02-07CH11358.

- [1] M. Rotter, M. Tegel, and D. Johrendt, *Phys. Rev. Lett.* **101**, 107006 (2008).
- [2] Y. Kamihara, T. Watanabe, M. Hirano, and H. Hosono, *J. Am. Chem. Soc.* **130**, 3296 (2008).
- [3] A. S. Sefat, R. Jin, M. A. McGuire, B. C. Sales, D. J. Singh, and D. Mandrus, *Phys. Rev. Lett.* **101**, 117004 (2008).
- [4] L. J. Li, Y. K. Luo, Q. B. Wang, H. Chen, Z. Ren, Q. Tao, Y. K. Li, X. Lin, M. He, Z. W. Zhu, G. H. Cao, and Z. A. Xu, *New J. Phys.* **11**, 025008 (2009).
- [5] W. Schnelle, A. Leithe-Jasper, R. Gumeniuk, U. Burkhardt, D. Kasinathan, and H. Rosner, *Phys. Rev. B* **79**, 214516 (2009).
- [6] S. Jiang, H. Xing, G. Xuan, C. Wang, Z. Ren, C. Feng, J. Dai, Z. Xu, and G. Cao, *J. Phys.: Condens. Matter* **21**, 382203 (2009).
- [7] E. Colombier, S. L. Bud'ko, N. Ni, and P. C. Canfield, *Phys. Rev. B* **79**, 224518 (2009).
- [8] J. Paglione and R. L. Greene, *Nat. Phys.* **6**, 645 (2010).
- [9] P. C. Canfield and S. L. Bud'ko, *Ann. Rev. Condens. Matter Phys.* **1**, 27 (2010).
- [10] D. C. Johnston, *Adv. Phys.* **59**, 803 (2010).

- [11] G. R. Stewart, *Rev. Mod. Phys.* **83**, 1589 (2011).
- [12] L. Taillefer, *Ann. Rev. Condens. Matter Phys.* **1**, 51 (2010).
- [13] P. Monthoux, D. Pines, and G. G. Lonzarich, *Nature (London)* **450**, 1177 (2007).
- [14] M. R. Norman, *Science* **332**, 196 (2011).
- [15] E. Abrahams and Q. Si, *J. Phys.: Condens. Matter* **23**, 223201 (2011).
- [16] S. Kasahara, T. Shibauchi, K. Hashimoto, K. Ikeda, S. Tonegawa, R. Okazaki, H. Shishido, H. Ikeda, H. Takeya, K. Hirata, T. Terashima, and Y. Matsuda, *Phys. Rev. B* **81**, 184519 (2010).
- [17] S. Kasahara, H. J. Shi, K. Hashimoto, S. Tonegawa, Y. Mizukami, T. Shibauchi, K. Sugimoto, T. Fukuda, T. Terashima, Andriy H. Nevidomskyy, and Y. Matsuda, *Nature (London)* **486**, 382 (2012).
- [18] Y. Nakai, T. Iye, S. Kitagawa, K. Ishida, H. Ikeda, S. Kasahara, H. Shishido, T. Shibauchi, Y. Matsuda, and T. Terashima, *Phys. Rev. Lett.* **105**, 107003 (2010).
- [19] K. Hashimoto, K. Cho, T. Shibauchi, S. Kasahara, Y. Mizukami, R. Katsumata, Y. Tsuruhara, T. Terashima, H. Ikeda, M. A. Tanatar, H. Kitano, N. Salovich, R. W. Giannetta, P. Walmsley, A. Carrington, R. Prozorov, and Y. Matsuda, *Science* **336**, 1554 (2012).
- [20] M. A. Tanatar, K. Hashimoto, S. Kasahara, T. Shibauchi, Y. Matsuda, and R. Prozorov, *Phys. Rev. B* **87**, 104506 (2013).
- [21] S. Nandi, M. G. Kim, A. Kreyssig, R. M. Fernandes, D. K. Pratt, A. Thaler, N. Ni, S. L. Bud'ko, P. C. Canfield, J. Schmalian, R. J. McQueeney, and A. I. Goldman, *Phys. Rev. Lett.* **104**, 057006 (2010).
- [22] M. A. Tanatar, N. Ni, C. Martin, R. T. Gordon, H. Kim, V. G. Kogan, G. D. Samolyuk, S. L. Bud'ko, P. C. Canfield, and R. Prozorov, *Phys. Rev. B* **79**, 094507 (2009).
- [23] M. A. Tanatar, N. Ni, G. D. Samolyuk, S. L. Bud'ko, P. C. Canfield, and R. Prozorov, *Phys. Rev. B* **79**, 134528 (2009).
- [24] M. A. Tanatar, N. Ni, A. Thaler, S. L. Bud'ko, P. C. Canfield, and R. Prozorov, *Phys. Rev. B* **82**, 134528 (2010).
- [25] M. A. Tanatar, N. Ni, A. Thaler, S. L. Bud'ko, P. C. Canfield, and R. Prozorov, *Phys. Rev. B* **84**, 014519 (2011).
- [26] N. Ni, M. E. Tillman, J.-Q. Yan, A. Kracher, S. T. Hannahs, S. L. Bud'ko, and P. C. Canfield, *Phys. Rev. B* **78**, 214515 (2008).
- [27] J. Murphy, M. A. Tanatar, Hyunsoo Kim, W. Kwok, U. Welp, D. Graf, J. S. Brooks, S. L. Bud'ko, P. C. Canfield, and R. Prozorov, *Phys. Rev. B* **88**, 054514 (2013).
- [28] C. Liu, T. Kondo, R. M. Fernandes, A. D. Palczewski, E. D. Mun, N. Ni, A. N. Thaler, A. Bostwick, E. Rotenberg, J. Schmalian, S. L. Bud'ko, P. C. Canfield, and A. Kaminski, *Nat. Phys.* **6**, 419 (2010).
- [29] B. Shen, H. Yang, Z.-S. Wang, F. Han, B. Zeng, L. Shan, C. Ren, and H.-H. Wen, *Phys. Rev. B* **84**, 184512 (2011).
- [30] M. A. Tanatar, E. C. Blomberg, H. Kim, K. Cho, W. E. Straszheim, B. Shen, H.-H. Wen, and R. Prozorov, *arXiv:1106.0533*.
- [31] H. Q. Luo, Z. S. Wang, H. Yang, P. Cheng, X. Zhu, and H.-H. Wen, *Supercond. Sci. Technol.* **21**, 125014 (2008).
- [32] D. Watanabe, T. Yamashita, Y. Kawamoto, S. Kurata, Y. Mizukami, T. Ohta, S. Kasahara, M. Yamashita, T. Saito, H. Fukazawa, Y. Kohori, S. Ishida, K. Kihou, C. H. Lee, A. Iyo, H. Eisaki, A. B. Vorontsov, T. Shibauchi, and Y. Matsuda, *Phys. Rev. B* **89**, 115112 (2014).
- [33] K. Kihou, T. Saito, S. Ishida, M. Nakajima, Y. Tomioka, H. Fukazawa, Y. Kohori, T. Ito, S. Uchida, A. Iyo, C.-H. Lee, and H. Eisaki, *J. Phys. Soc. Jpn.* **79**, 124713 (2010).
- [34] N. Ni, S. L. Bud'ko, A. Kreyssig, S. Nandi, G. E. Rustan, A. I. Goldman, S. Gupta, J. D. Corbett, A. Kracher, and P. C. Canfield, *Phys. Rev. B* **78**, 014507 (2008).
- [35] S. Avci, O. Chmaissem, E. A. Goremychkin, S. Rosenkranz, J.-P. Castellan, D. Y. Chung, I. S. Todorov, J. A. Schlueter, H. Claus, M. G. Kanatzidis, A. Daoud-Aladine, D. Khalyavin, and R. Osborn, *Phys. Rev. B* **83**, 172503 (2011).
- [36] S. Avci, O. Chmaissem, D. Y. Chung, S. Rosenkranz, E. A. Goremychkin, J. P. Castellan, I. S. Todorov, J. A. Schlueter, H. Claus, A. Daoud-Aladine, D. D. Khalyavin, M. G. Kanatzidis, and R. Osborn, *Phys. Rev. B* **85**, 184507 (2012).
- [37] M. Rotter, M. Pangerl, M. Tegel, and D. Johrendt, *Angew. Chem. Int. Ed.* **47**, 7949 (2008).
- [38] A. A. Golubov, O. V. Dolgov, A. V. Boris, A. Charnukha, D. L. Sun, C. T. Lin, A. F. Shevchun, A. V. Korobenko, M. R. Trunin, and V. N. Zverev, *JETP Lett.* **94**, 333 (2011).
- [39] J. K. Dong, S. Y. Zhou, T. Y. Guan, H. Zhang, Y. F. Dai, X. Qiu, X. F. Wang, Y. He, X. H. Chen, and S. Y. Li, *Phys. Rev. Lett.* **104**, 087005 (2010).
- [40] T. Terashima, M. Kimata, H. Satsukawa, A. Harada, K. Hazama, S. Uji, H. Harima, G.-F. Chen, J.-L. Luo, and N.-L. Wang, *J. Phys. Soc. Jpn.* **78**, 063702 (2009).
- [41] K. Hashimoto, A. Serafin, S. Tonegawa, R. Katsumata, R. Okazaki, T. Saito, H. Fukazawa, Y. Kohori, K. Kihou, C. H. Lee, A. Iyo, H. Eisaki, H. Ikeda, Y. Matsuda, A. Carrington, and T. Shibauchi, *Phys. Rev. B* **82**, 014526 (2010).
- [42] J.-Ph. Reid, M. A. Tanatar, A. Juneau-Fecteau, R. T. Gordon, S. R. de Cotret, N. Doiron-Leyraud, T. Saito, H. Fukazawa, Y. Kohori, K. Kihou, C. H. Lee, A. Iyo, H. Eisaki, R. Prozorov, and L. Taillefer, *Phys. Rev. Lett.* **109**, 087001 (2012).
- [43] Y. Liu, M. A. Tanatar, V. G. Kogan, Hyunsoo Kim, T. A. Lograsso, and R. Prozorov, *Phys. Rev. B* **87**, 134513 (2013).
- [44] Y. M. Dai, B. Xu, B. Shen, H. Xiao, H. H. Wen, X. G. Qiu, C. C. Homes, and R. P. S. M. Lobo, *Phys. Rev. Lett.* **111**, 117001 (2013).
- [45] V. A. Gasparov, F. Wolff-Fabris, D. L. Sun, C. T. Lin, and J. Wosnitzer, *JETP Lett.* **93**, 26 (2011).
- [46] H. Q. Yuan, J. Singleton, F. F. Balakirev, S. A. Baily, G. F. Chen, J. L. Luo, and N. L. Wang, *Nature (London)* **457**, 565 (2009).
- [47] Z.-S. Wang, H.-Q. Luo, C. Ren, and H.-H. Wen, *Phys. Rev. B* **78**, 140501(R) (2008).
- [48] D. A. Zocco, K. Grube, F. Eilers, T. Wolf, and H. v. Löhneysen, *Phys. Rev. Lett.* **111**, 057007 (2013).
- [49] S. Kittaka, Y. Aoki, N. Kase, T. Sakakibara, T. Saito, H. Fukazawa, Y. Kohori, K. Kihou, C.-H. Lee, A. Iyo, H. Eisaki, K. Deguchi, N. K. Sato, Y. Tsutsumi, and K. Machida, *J. Phys. Soc. Jpn.* **83**, 013704 (2014).
- [50] A. I. Larkin and Yu. N. Ovchinnikov, *Sov. Phys. JETP* **20**, 762 (1965).
- [51] P. Fulde and R. A. Ferrell, *Phys. Rev.* **135**, A550 (1964).
- [52] M. Takahashi, T. Mizushima, and K. Machida, *Phys. Rev. B* **89**, 064505 (2014).
- [53] T. Terashima, K. Kihou, M. Tomita, S. Tsuchiya, N. Kikugawa, S. Ishida, C.-H. Lee, A. Iyo, H. Eisaki, and S. Uji, *Phys. Rev. B* **87**, 184513 (2013).

- [54] M. A. Tanatar, N. Ni, S. L. Bud'ko, P. C. Canfield, and R. Prozorov, *Supercond. Sci. Technol.* **23**, 054002 (2010).
- [55] M. A. Tanatar, R. Prozorov, N. Ni, S. L. Bud'ko, and P. C. Canfield, US Patent 8, 450, 246.
- [56] J. T. Park, D. S. Inosov, Ch. Niedermayer, G. L. Sun, D. Haug, N. B. Christensen, R. Dinnebier, A. V. Boris, A. J. Drew, L. Schulz, T. Shapoval, U. Wolff, V. Neu, X. Yang, C. T. Lin, B. Keimer, and V. Hinkov, *Phys. Rev. Lett.* **102**, 117006 (2009).
- [57] W. K. Yeoh, B. Gault, X. Y. Cui, C. Zhu, M. P. Moody, L. Li, R. K. Zheng, W. X. Li, X. L. Wang, S. X. Dou, G. L. Sun, C. T. Lin, and S. P. Ringer, *Phys. Rev. Lett.* **106**, 247002 (2011).
- [58] L. Shan, Y.-L. Wang, B. Shen, B. Zeng, Y. Huang, A. Li, D. Wang, H. Yang, C. Ren, Q.-H. Wang, S. H. Pan, and H.-H. Wen, *Nat. Phys.* **7**, 325 (2011).
- [59] C.-L. Song, Y. Yin, M. Zech, T. Williams, M. M. Yee, G.-F. Chen, J.-L. Luo, N.-L. Wang, E. W. Hudson, and J. E. Hoffman, *Phys. Rev. B* **87**, 214519 (2013).
- [60] F. Rullier-Albenque, D. Colson, A. Forget, and H. Alloul, *Phys. Rev. Lett.* **103**, 057001 (2009).
- [61] N. Xu, P. Richard, X. Shi, A. van Roekeghem, T. Qian, E. Razzoli, E. Rienks, G.-F. Chen, E. Ieki, K. Nakayama, T. Sato, T. Takahashi, M. Shi, and H. Ding, *Phys. Rev. B* **88**, 220508 (2013).
- [62] N. Doiron-Leyraud, P. Auban-Senzier, S. René de Cotret, C. Bourbonnais, D. Jérôme, K. Bechgaard, and L. Taillefer, *Phys. Rev. B* **80**, 214531 (2009).
- [63] L. P. Gor'kov and T. K. Melik-Barkhudarov, *Sov. Phys. JETP* **18**, 1031 (1964).
- [64] J. Murphy, M. A. Tanatar, D. Graf, J. S. Brooks, S. L. Bud'ko, P. C. Canfield, V. G. Kogan, and R. Prozorov, *Phys. Rev. B* **87**, 094505 (2013).
- [65] M. M. Altarawneh, K. Collar, and C. H. Mielke, N. Ni, S. L. Bud'ko, and P. C. Canfield, *Phys. Rev. B* **78**, 220505 (2008).
- [66] U. Welp, R. Xie, A. E. Koshelev, W. K. Kwok, H. Q. Luo, Z. S. Wang, G. Mu, and H.-H. Wen, *Phys. Rev. B* **79**, 094505 (2009).
- [67] A. M. Clogston, *Phys. Rev. Lett.* **9**, 266 (1962); B. S. Chandrasekhar, *Appl. Phys. Lett.* **1**, 7 (1962).
- [68] N. R. Werthamer, E. Helfand, and P. C. Hohenberg, *Phys. Rev.* **147**, 295 (1966).
- [69] J.-P. Castellan, S. Rosenkranz, E. A. Goremychkin, D. Y. Chung, I. S. Todorov, M. G. Kanatzidis, I. Eremin, J. Knolle, A. V. Chubukov, S. Maiti, M. R. Norman, F. Weber, H. Claus, T. Guidi, R. I. Bewley, and R. Osborn, *Phys. Rev. Lett.* **107**, 177003 (2011).
- [70] C. H. Lee, K. Kihou, H. Kawano-Furukawa, T. Saito, A. Iyo, H. Eisaki, H. Fukazawa, Y. Kohori, K. Suzuki, H. Usui, K. Kuroki, and K. Yamada, *Phys. Rev. Lett.* **106**, 067003 (2011).
- [71] M. Hirano, Y. Yamada, T. Saito, R. Nagashima, T. Konishi, T. Toriyama, Y. Ohta, H. Fukazawa, Y. Kohori, Y. Furukawa, K. Kihou, C.-H. Lee, A. Iyo, and H. Eisaki, *J. Phys. Soc. Jpn.* **81**, 054704 (2012).
- [72] M. Kano, Y. Kohama, D. Graf, F. Balakirev, A. S. Sefat, M. A. Mcguire, B. C. Sales, D. Mandrus, and S. W. Tozer, *J. Phys. Soc. Jpn.* **78**, 084719 (2009).
- [73] J. Jaroszynski, F. Hunte, L. Balicas, Youn-jung Jo, I. Raičević, A. Gurevich, D. C. Larbalestier, F. F. Balakirev, L. Fang, P. Cheng, Y. Jia, and H. H. Wen, *Phys. Rev. B* **78**, 174523 (2008).
- [74] K. Cho, H. Kim, M. A. Tanatar, Y. J. Song, Y. S. Kwon, W. A. Coniglio, C. C. Agosta, A. Gurevich, and R. Prozorov, *Phys. Rev. B* **83**, 060502(R) (2011).
- [75] S. Khim, J. W. Kim, E. S. Choi, Y. Bang, M. Nohara, H. Takagi, and K. H. Kim, *Phys. Rev. B* **81**, 184511 (2010).
- [76] M. Fang, J. Yang, F. F. Balakirev, Y. Kohama, J. Singleton, B. Qian, Z. Q. Mao, H. Wang, and H. Q. Yuan, *Phys. Rev. B* **81**, 020509 (2010).
- [77] N. Ni, J. M. Allred, B. C. Chan, and R. J. Cava, *Proc. Natl. Acad. Sci. USA* **108**, E1019 (2011).
- [78] U. Welp, C. Chaparro, A. E. Koshelev, W. K. Kwok, A. Rydh, N. D. Zhigadlo, J. Karpinski, and S. Weyeneth, *Phys. Rev. B* **83**, 100513(R) (2011).
- [79] G. Li, G. Grissonnanche, J.-Q. Yan, R. W. McCallum, T. A. Lograsso, H. D. Zhou, and L. Balicas, *Phys. Rev. B* **86**, 054517 (2012).
- [80] V. G. Kogan and R. Prozorov, *Rep. Prog. Phys.* **75**, 114502 (2012).
- [81] H. Ding, P. Richard, K. Nakayama, K. Sugawara, T. Arakane, Y. Sekiba, A. Takayama, S. Souma, T. Sato, T. Takahashi, Z. Wang, X. Dai, Z. Fang, G. F. Chen, J. L. Luo, and N. L. Wang, *Europhys. Lett.* **83**, 47001 (2008).
- [82] T. Sato, K. Nakayama, Y. Sekiba, P. Richard, Y.-M. Xu, S. Souma, T. Takahashi, G. F. Chen, J. L. Luo, N. L. Wang, and H. Ding, *Phys. Rev. Lett.* **103**, 047002 (2009).
- [83] W. Malaeb, T. Shimojima, Y. Ishida, K. Okazaki, Y. Ota, K. Ohgushi, K. Kihou, T. Saito, C. H. Lee, S. Ishida, M. Nakajima, S. Uchida, H. Fukazawa, Y. Kohori, A. Iyo, H. Eisaki, C.-T. Chen, S. Watanabe, H. Ikeda, and S. Shin, *Phys. Rev. B* **86**, 165117 (2012).
- [84] A. Gurevich, *Rep. Prog. Phys.* **74**, 124501 (2011).
- [85] V. G. Kogan, *Phys. Rev. B* **80**, 214532 (2009).
- [86] J.-Ph. Reid, A. Juneau-Fecteau, R. T. Gordon, S. René de Cotret, N. Doiron-Leyraud, X. G. Luo, H. Shakeripour, J. Chang, M. A. Tanatar, H. Kim, R. Prozorov, T. Saito, H. Fukazawa, Y. Kohori, K. Kihou, C. H. Lee, A. Iyo, H. Eisaki, B. Shen, H.-H. Wen, and Louis Taillefer, *Supercond. Sci. Technol.* **25**, 084013 (2012).
- [87] R. Prozorov, K. Cho, H. Kim, and M. A. Tanatar, *J. Phys.: Conf. Ser.* **449**, 012020 (2013).